LASER & PHOTONICS REVIEWS
www.lpr-journal.org

Direct Monitoring of Whole-Brain Electrodynamics via High-Spatiotemporal-Resolution Photoacoustics with Voltage-Sensitive Dye

Weiran Pang, Bowen Zhu, Honghui Li, Yingying Zhou, Chi Man Woo, Xiazi Huang, Tianting Zhong, Hsuan Lo, Laiyou Wang, Puxiang Lai, and Liming Nie**

Brain voltage plays a crucial role in indicating internal functions or diseases, and optical voltage imaging has gained intensive attention in recent years. Despite encouraging progress, current implementations encounter limitations pertaining to penetration depth, field of view (FOV), and photostability of indicators. To mitigate these challenges, a robust voltage-sensitive dye (VSD)-based whole-field photoacoustic brain detection (WF-PABD) platform is proposed, enabling direct evaluation of voltage dynamics across the whole brain, forming as PA-VSD. WF-PABD is equipped with a 512-element ring-array ultrasound detector capable of 360-degree scanning, providing a large FOV (≈5 cm), high spatial resolution (≈110 µm), and rapid imaging acquisition. The proposed VSD remained ≈75% photostability after 30 min laser exposure, much greater than most calcium sensors. The optical voltage-response mechanisms are validated and the capability of PA-VSD to directly screen seizures is established. It is demonstrated that investigating connectivity among different brain regions allows to identify the precise location of active epileptic foci as well as the electrical conduction pathways and their directionality through fast temporal visualization. In summary, this study not only addresses the need for non-invasive, high-resolution, long-term, and direct monitoring of brain voltage but also empowers exciting venues for PA applications in neuroscience.

1. Introduction

The communication of electrical signals among vast populations of neurons in numerous regions is essential for studying brain function and diseases. A comprehensive knowledge of the time-varying activity of the whole brain at various spatial scales and depths is desired. Nowadays, research on abnormal neuron discharge has been conducted for central nervous system disorders, such as epilepsy. In clinical manifestation, a seizure is characterized by aberrant synchronized firing of the hyperexcitable population of cortical neurons,[1] which can be life-threatening in severe cases. Hence, prolonged monitoring of whole-brain voltage dynamics can promote the assessment of illness development and enable prompt and precise therapy.

To explore spontaneous neurotransmitter events generated by voltage fluctuations in the pathophysiological state, membrane potential studies via electrical recording or optical imaging

W. Pang, H. Li, H. Lo, L. Wang, L. Nie
Medical Research Institute
Guangdong Provincial People's Hospital (Guangdong Academy of Medical Sciences)
Southern Medical University
Guangzhou 510080, China
E-mail: nieliming@gdph.org.cn

W. Pang, Y. Zhou, C. M. Woo, X. Huang, T. Zhong, P. Lai
Department of Biomedical Engineering
The Hong Kong Polytechnic University
Hong Kong SAR, China
E-mail: puxiang.lai@polyu.hk.edu

P. Lai
Photonics Research Institute
The Hong Kong Polytechnic University
Hong Kong SAR, China

P. Lai
Joint Research Centre for Biosensing and Precision Theranostics
The Hong Kong Polytechnic University
Hong Kong SAR, China

L. Nie
Department of Biomedical Engineering
Southern Medical University
Guangzhou 510515, China

The ORCID identification number(s) for the author(s) of this article can be found under https://doi.org/10.1002/lpor.202400165

DOI: 10.1002/lpor.202400165

with voltage-sensitive dye (VSD) have been developed.[2–4] In practice, the patch-clamp technique[5] is the gold standard for detecting cell membrane potentials with good accuracy in vitro, yet it is still difficult to accomplish in vivo. Electroencephalography (EEG)[6] is another technique frequently used to track the brain's electrical activities. Still, the reliance on the number and spatial distribution of electrodes makes it challenging to achieve high spatial resolution. Recently, the combination of super-resolution fluorescence (FL) microscopy (especially two-photon microscopy, 2PM) and near-infrared genetically encoded calcium indicators (GECIs) acts as a preference for visualizing brain voltage. It is now possible to measure the action potential of cortical neurons in conscious animals with a super high resolution,[7–11] which, however, can only be carried out in a very narrow field of view (FOV) at a superficial layer, e.g., an investigation with a dozen neurons at a depth of hundreds of microns.[12] Due to light scattering of overlying tissues, these optical detection methods, which are comparable to 2PM, have a limited FOV and shallow penetration depth. Although multiphoton can extend the depth of imaging, it is only by ≈1 mm at most.[11] The demand for wide-field, deep-penetrating, high-resolution, and high-speed monitoring of neural voltage dynamics in the brain is yet to be addressed.

Photoacoustic (PA) imaging, also termed optoacoustic imaging, is an emerging hybrid imaging technique that can non-invasively identify tissue with high specificity and micron-scale resolution at increased penetration depth. It employs a pulsed laser as the excitation source and gathers the ultrasonic response to get the light absorption maps of structural and functional information of the target tissue, well eliminating the negative effects of light scattering within the tissue.[13–20] The vascular specificity of PA imaging assists in the neurovascular coupling of neural voltage imaging, as evidenced by numerous studies in recent years.[21,22] However, these studies typically interrogate neuronal voltage activities through vascular and blood oxygenation fluctuations rather than direct measurement. In 2019, Sven Gottschalk et al. attempted to understand deep-area voltage activity by combining GCaMP6-family GECI with PA imaging, opening a new venue for rapid and high-resolution monitoring of neuronal action potentials throughout the brain.[23] Nevertheless, the weak photostability of GCaMP dyes makes them unsuitable for tracking the whole-brain voltage activity over extended periods (usually requiring brain recordings of at least 30 min).[24,25] Moreover, because of its cell-type specificity dependency, there might be poor response out of the scope. Taking into account the gene-encoded ethics, the GECI-based implementations have limited applicability for clinics.

In this work, we propose a novel strategy, that employs a whole-field photoacoustic brain detection (WF-PABD) platform adapted with a photostable VSD (PA-VSD), to directly monitor voltage dynamics over 30 min (even longer if needed) in an intact epileptic mouse brain. A methodology is developed to utilize PA data analysis to provide identification and screening of epileptic signals. Regarding system validation, WF-PABD possesses a vast FOV of ≈5 cm in diameter for enough to cover the whole mouse brain, a high spatial resolution of ≈110 μm, a fast imaging rate of 10 Hz, and a deep penetrating depth covering all areas of interest. Following in-vitro cell experiments and in-vivo fluorescent investigations, the optical features of voltage response and the mechanism of VSD can be verified and then confirmed in the fluctuations of PA signals. PA-VSD localized epilepsy foci and screened seizure dynamics non-invasively, as well as offered guidance on electrical conduction pathways and functional communications across brain regions. Through multiple data processing, it can be discovered that epileptic signals contain more high-frequency components than calm signals. Moreover, there exists a close correlation between the change rates (CRs) and high-frequency amplitudes of PA signals, showing a peak-to-peak pairing feature. It is anticipated that a new methodology can be established by capturing the CRs and discrete high-frequency amplitudes (DHF) coupling to screen epileptic sequences. The results highlight the potential of PA-VSD as a high-spatiotemporal-resolution tool for in-depth analysis of brain voltage dynamics. It is expected that the platform might serve as a springboard for further research in photoacoustic neuroscience and neuropathophysiology.

2. Results

2.1. WF-PABD Achieves High-Spatiotemporal-Resolution Screening of the Whole Brain

A simplified schematic of the WF-PABD system is illustrated in **Figure 1a**. In this system, we employed a wideband laser (Q-smart 450, Quantel laser, France) with output wavelengths ranging from 670 to 980, 1064, and 1190 to 2600 nm, operating at a laser repetition rate of 10 Hz. The pulsed light was amplified through a concave lens (LD1357, Thorlabs, USA) and uniformly irradiated onto the mouse head. High-speed PA signal detection was achieved using a fully circular ultrasonic transducer array consisting of 512 elements (Imasonic, France). The diameter of the ultrasonic ring array was ≈10 cm, with a central frequency of 5.5 MHz and a bandwidth of 9.9 MHz (>90%). A transparent glass was placed above the ultrasonic ring array chamber, while a layer of cling film was applied beneath it. The chamber was filled with water using a pump, and a negative pressure method was employed to create a concave groove in the cling film. An anesthetized mouse was fixed in the concave groove using a holder, and the head was tightly coupled to the water chamber using ultrasound-coupling gel. This water medium facilitated acoustic coupling and ensured the propagation of PA signals. Subsequently, a 512-channel data acquisition system (DAQs, Photosound, USA) with a sampling rate of 40 MSa s^{-1} was utilized to simultaneously receive the PA signals in parallel, which warrantied an ultrafast imaging acquisition time (≈10 μs per frame) to avoid respiratory and motion artifacts.

The PA platform used a laser with an excitation wavelength of 670 nm and a single pulse energy of about 100 mJ. An average laser fluence of 56 mJ cm^{-2} is calculated when the spot size over the entire mouse brain is taken into account, and this falls inside the photodamage threshold.[26,27] The detections occurred with a 40 dB gain in the following investigations. In a phantom experiment, the system was characterized to have a vast imaging range

B. Zhu
Department of Anaesthesia and Perioperative Medicine
Henan University People's Hospital
People's Hospital of Zhengzhou University
Henan Provincial People's Hospital
Zhengzhou 450003, China

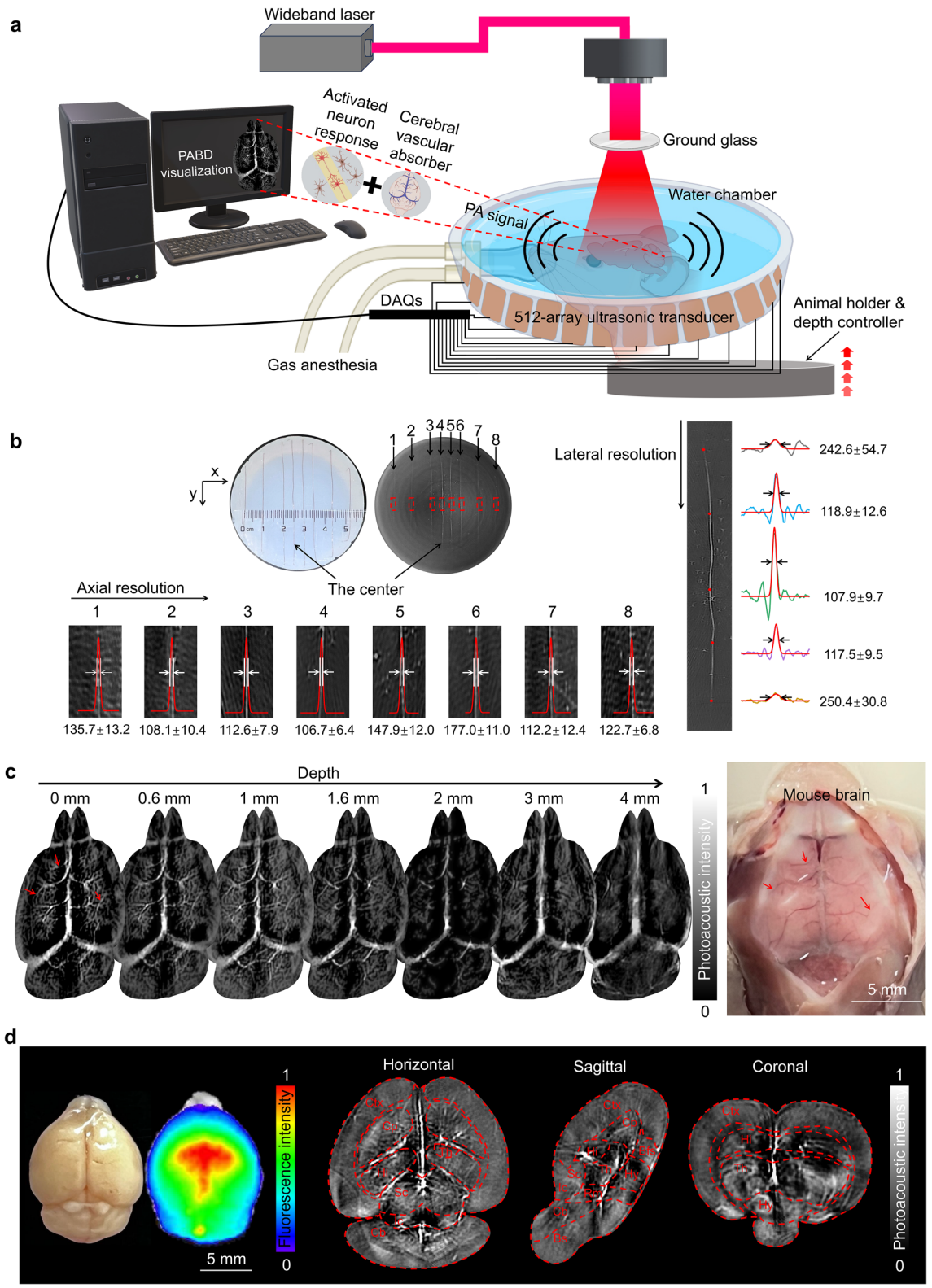

Figure 1. Schematic of the experimental system setup and a high-resolution photoacoustic visualization of the mouse brain. a) WF-PABD implementations. PA signals come from a stronger neuron response via VSDs and weaker blood absorption. b) Evaluation of the axial and lateral resolutions. The units are microns. c) Intravital visualization of the whole mouse brain at different depths (side-view with X: 310° Y: 10°). d) Images of isolated brain tissue carrying DiSC3(5) provide structural details in the horizontal, sagittal, and coronal sections and contour lines for several brain regions. Reference from Mouse Brain Atlas (75, 152, 264). Ctx: Cerebral Cortex; Cp: Caudata Putamen; Hi: Hippocampal; Th: Thalamus; Sc: Superior Colliculi; Ic: Inferior Colliculi; Bfs: Basal Forebrain Septum; Hy: Hypothalamus; Rm: Rest of Midbrain; Cb: Cerebellum; Bs: Brain Stem.

of ≈5 cm in diameter and a lateral resolution of <110 μm at the center, and ≈250 μm at the distal end. The axial resolution was also best at the center and gradually decreased away from the center (Figure 1b). During in vivo detection, a mouse was placed on a holding platform and its head was secured with ear rods and anesthetized with a mask for prolonged respiratory anesthesia (isoflurane, 1% VOL, gas flow rate of 1 cm^3 s^{-1}). An elevator was placed below to control movement and scanning of mouse brain in the elevational direction. We set the top horizontal section of the mouse cerebral cortex as the 0-depth plane and non-invasively captured the brain images of the live mouse with an injection of DiSC3(5) through the tail vein. The vascular and brain structures at different depths (0–4 mm) are displayed in Figure 1c. After the experiment, the mouse scalp was opened, and the cortex was imaged with a camera. It was found that the reconstructed PA brain vascular structures perfectly matched the actual vascular structure, even for the tiny blood vessels at the edges (indicated by the red arrows in Figure 1c). Following the mouse cardiac perfusion procedure, the brain (without blood) was preserved and fixed in paraformaldehyde. The visible fluorescence signal indicated that DiSC3(5) was present in the brain parenchyma. Then, the brain images in horizontal, sagittal, and coronal sections were obtained. It can be observed that several functional regions, such as the cortex, hippocampus, et al, can be identified from the PA images (Figure 1d). It shows that despite the absence of blood uptake, VSDs were still able to provide signals of sufficient contrast for brain image capturing. All those results suggested the advantages of PA-VSD, such as vast FOV, high spatiotemporal resolution, sufficient contrast, and functional information readout capabilities.

2.2. DiSC3(5) Exhibits Excellent FL and PA Voltage Response

A VSD named DiSC3(5), 3-propyl-2-(5-(3-propyl)-2(3H)-benzothiazolidene-1,3-pentadienyl), that is a kind of carbocyanine previously used to evaluate mitochondrial membrane potential was employed for in-vivo measurements in this work.[28,29] We discovered that DiSC3(5) has demonstrated both excellent fluorescence and photoacoustic signaling capabilities. It has an absorption peak at 656 nm (**Figure 2a**), and the absorption increases almost linearly (R^2 = 0.99957) with the concentration (Figure 2b). Cell Counting Kit-8 (CCK8) was used for cell proliferation and toxicity research to confirm its safety. The results show that it is biosafe at the highest blood-level concentration employed in in-vivo trials (Figure S1, Supporting Information). Hence, there were no toxicity concerns in cellular as well as in-vivo animal experiments since the concentration of DiSC3(5) that diffuses to the brain will be even lower. To test the ability of DiSC3(5) to sense voltage, an identical number of HEK-293T cells were seeded in a 96-well plate. After one day of culture, the wells were divided into 4 groups (each column acted as one group) and then filled with extracellular medium with 3, 1.5, 0.75, and 0.375 μM DiSC3(5) solution, respectively. Valinomycin (Val) was added to the first row and Gramicidin (Gra) was added to the second row to simulate the polarized and depolarized state of the cells, respectively, while the third row served as the control (Figure S2a–d, Supporting Information). The optical absorption peaks at different concentrations of DiSC3(5) were shown in the bar graphs (Figure S2e, Supporting Information). Lower absorbance was observed in the Val group, which is consistent with the theory that the voltage indicators exhibit lower absorbance in the polarized state of cells. This confirmed the ability of DiSC3(5) to respond to voltage changes at in-vitro level.

Flow cytometry assays were carried out to confirm that DiSC3(5) had the capacity to actively penetrate neuronal cell membranes and generate fluorescent signals upon entrance into cells. Here, Neuro-2a (N2a) cells were employed. The results revealed that the DiSC3(5) group (Figure 2d) had a very strong FL signal while the control group (Figure 2c, without the dye) had none, showing that the co-cultured DiSC3(5)-containing cells were the sources of the main FL signal, but not the free dyes. Then, the membrane potential was modulated by adjusting the K+ concentration of the extracellular medium (estimated by the Nernst equation), and meanwhile, optical properties of DiSC3(5) were measured, which reflected the changes of FL and PA signal. This allowed us to investigate connection and regularity between the FL and PA signal transformations of DiSC3(5) at different cell membrane potentials. A small animal fluorescence imaging system (IVIS Spectrum In vivo Imaging System, Perkin Elmer, USA) was used to capture the FL images (Figure 2e). The signal increases with the advancing membrane potential, representing an enhancement in FL intensity with an expansion in depolarization, according to the statistical and quantitative analysis with regions of interest (ROI) of whole wells (Figure 2f, $n = 3$).

Following laser irradiation of the DiSC3(5) aqueous solution (concentration of 100 μM with 1% DMSO, Dimethyl sulfoxide), the optical absorption ratio was examined to evaluate the photobleaching effect (Figure 2g), and the absorption peak and ratio at 670 nm were individually recorded (Figure 2h, $n = 3$). It can be observed that DiSC3(5) retained ≈75% of its optical absorption intensity after being continuously exposed to a pulsed laser for 30 min. Given this property, DiSC3(5) was exposed to relatively low laser energy due to light scattering and absorption by skin and tissue during in-vivo small animal tests, making it less susceptible to photobleaching. This means that DiSC3(5) has more stable optical properties than most GEVIs, which is one of the most crucial qualifications for long-term in vivo monitoring.[23]

To check whether its PA effect also corresponds to the voltage change, photoacoustic microscopy (PAM) imaging was conducted to find DiSC3(5) variations in N2a's PA signal. Several PA images were captured under the G2 OR-PAM system (INNO LASER, China), with a scanning step size of 3 μm and an imaging area of 900 × 900 $μm^2$. The cells were clearly seen thanks to the high resolution (Figure 2i), and the black dashed circle showed the contour of one single cell (top left). A self-written contour extraction algorithm was applied to the original image matrix, and the longest diameter of the contour was taken for computation and statistical analysis (Figure S3a, Supporting Information). As can be seen, the majority of the cells have a diameter of ≈20 μm, which is consistent with the actual diameter of the N2a cell. The average full-width half-maximum (FWHM) of the PA measurements in Figure S3b,c (showing the A-line with the largest diameter among 10 randomly selected cells) further supported the accuracy of this observation. The PA signal steadily reduced as the resting potential was increased. The cell shape shrank and developed more hollow structures, which also suggested that the

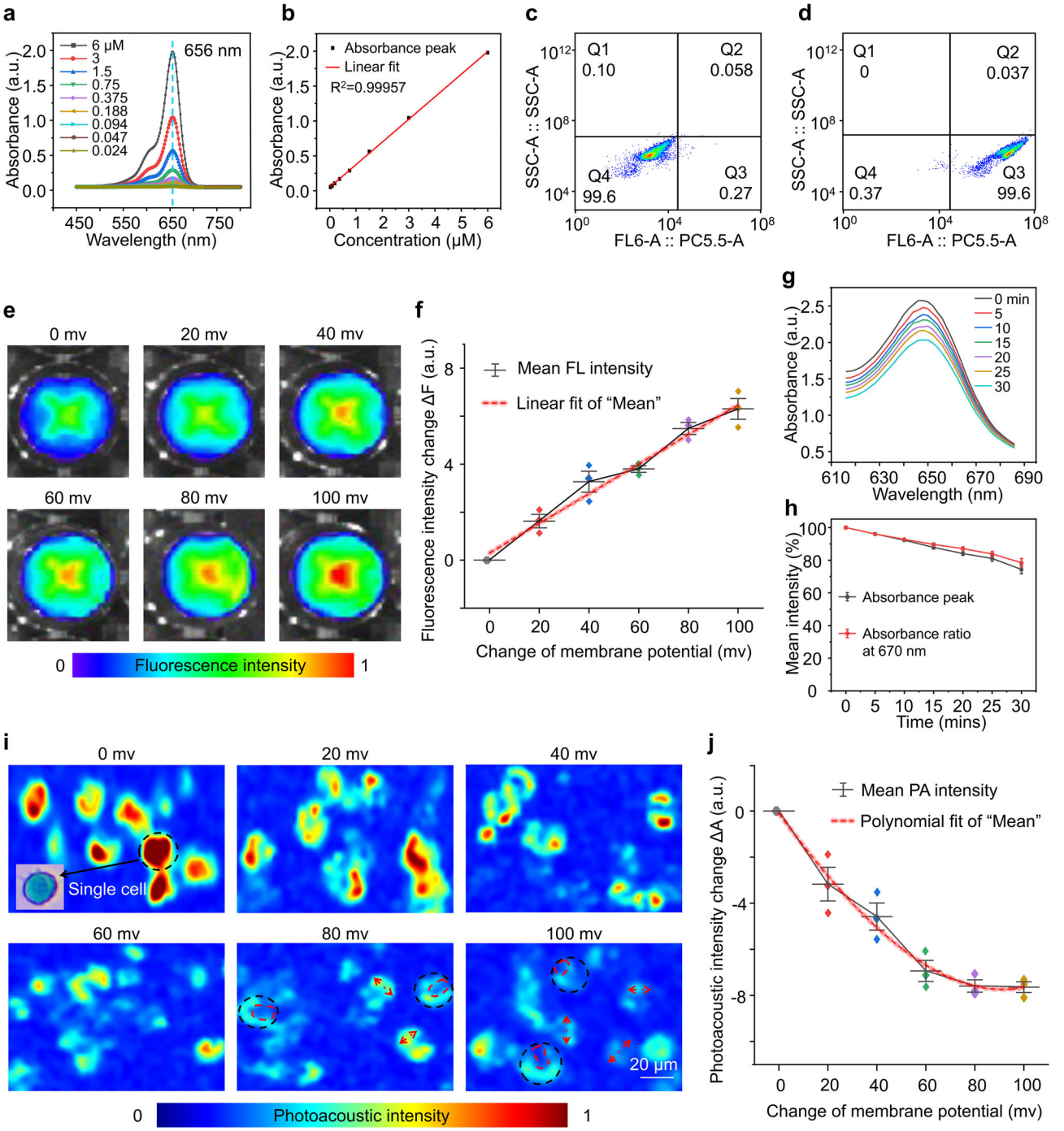

Figure 2. In vitro examination of the voltage response appearances of DiSC3(5). a) Absorption spectra of DiSC3(5). b) Absorption calibration curve as a function of DiSC3(5) concentration. c) Flow cytometry of neuronal cells without DiSC3(5). d) Flow cytometry of neuronal cells with DiSC3(5). e) FL imaging of N2a with DiSC3(5) at different resting membrane potentials. f) Quantitative analysis of FL amplitude over the full FOV. g) Absorption spectra of DiSC3(5) solutions under different durations of laser irradiation. h) The statistics of the absorption peak and the absorption ratio at 670 nm. i) PAM imaging of N2a with DiSC3(5) at different resting membrane potentials. j) Quantitative analysis of PA amplitude. All the error bar in the figures is SEM.

dispersion of DiSC3(5) resulted in a decreased PA signal. Subsequently, the mean single-pixel intensity was calculated to reflect the average PA intensity at the different resting potentials using the images with similar cell densities ($n = 3$ in each group). As the potential changed, the results revealed a progressive drop in PA intensity (Figure 2j). We found that the PA response trended in the opposite direction of FL, which is in accordance with the rule of energy conservation. The coexistence of an increase in FL signal and a decrease in PA signal accompanies the appearance of nerve cell depolarization.

2.3. DiSC3(5) Reacts Directly to Voltage Through Fluorescent and Photoacoustic Intensity Changes

Most chromophores reach an excited state following absorbance of photons but release energy in the form of heat or emit other photons when the excited atoms return to their ground state. In this manner, the emitted photons may be detected as FL signals or the converted heat generates ultrasonic waves that can be detected as PA signals, which align well with the principle of energy conservation. The cyanine dyes like DiSC3(5) are prone to agglomerate at high concentrations. There is weaker or no fluorescence in the aggregates, which is called fluorescent quench.[30] The principle of DiSC3(5) responding voltage via FL and PA changes is that cationic DiSC3(5) molecules can be actively attracted into the polarized cell at negative potentials and driven to aggregates by sufficiently high local concentrations, resulting in weaker-fluorescent aggregates, but the photoacoustic effect is instead enhanced. When depolarization occurs, the aggregates are freed into monomers and emitted outside the cell with the ions flow, thus turning into fluorescent but weaker photoacoustic monomers (**Figure 3a**). This process is reversible and repeatable. This is because the onset of repolarization drives the dye monomers into the cell interior again and maintains the tendency for dye aggregation.

Other materials have also shown similar optical characteristics in earlier investigations.[31] Yet few have conducted meaningful studies on live animals' deep brains. Therefore, we propose an innovative attempt to use DiSC3(5) in the prolonged monitoring of electrodynamics in epileptic mice (longer than 30 mins). Figure 3b illustrates the flowchart of this work. Continuous injection of low-dose PTZ is a classical method for epilepsy modeling. In our modeling, we found that the survival rate was higher than 80%. The effectiveness of the models was demonstrated by acute and enormous EEG spikes (Figure S4a, Supporting Information) as well as aberrant neuronal lesions in the cortex and hippocampus area (Figure S5, Supporting Information). When epileptic mice carrying DiSC3(5) triggered seizures, both fluorescent and photoacoustic modes were used to detect voltage response. Their FL and PA signal changes can directly reflect the voltage dynamic fluctuations of the mouse brain. Therefore, a method can be established to localize the lesions, screen the epileptic signals, and quantify the regularity and features of the statistical signals.

2.4. Fluorescence Imaging Validates Epileptic Response In Vivo Via DiSC3(5)

Here, we established the epileptic mouse model and performed FL imaging in vivo to detect the ability of DiSC3(5) that respond to the voltage dynamics in the cortex. With at least three animals in each group, three groups were set up for in vivo FL imaging: an epileptic voltage response group (DiSC3(5) + PTZ), a non-epileptic voltage response group (DiSC3(5) + NS, NS is the normal saline), and an epileptic non-voltage response group (ICG + PTZ). After injection of DiSC3(5) solution through the tail vein, the animals were observed at rest for two hours, with an excitation at 640 nm and an emission at 680 nm. It can be seen that the FL signal peaked at 5 min (**Figure 4a**, 125th min before injection) and then declined gradually until reaching a relatively stable condition (−40–0 min), which was caused by a number of factors. Firstly, DiSC3(5) entered the nerve cells, generated aggregation under the action of negative potential, and temporarily quenched the FL. Secondly, extra probes were disseminated throughout the brain with the blood flow and metabolized away. Thirdly, a tiny number of probes were photobleached upon slight light stimulation. All mice were subjected to FL image capture with anesthetized and immobilized heads. We utilized a PTZ injection to induce seizures, with a dosage four times greater than that used in the epilepsy modeling, since anesthesia might significantly reduce neuronal activity and the probability of seizures (Figure S4b, Supporting Information).[32]

An intraperitoneal injection of PTZ or saline was administered, followed by continuous recording at a rate of one frame per minute (Figure 4a, 30 min after injection). We discovered that the DiSC3(5) + PTZ group exhibited clear feedback of FL signal fluctuations through quantitative statistical ROI analysis. Within ≈2 min, the signal began to elevate, reaching its peak at 15 min, followed by a gradual decline and stabilization after 20 min (Figure 4b). Seizure peak periods were identified as those exceeding the linear growth trend. However, due to the limited temporal resolution of in-vivo FL imaging, only vague time intervals could be observed. The time-varying curves for the three groups are shown in Figure 4c,d. The two curves without brain voltage response (DiSC3(5) + NS and ICG + PTZ) exhibited significant differences in their trends when compared to the epilepsy group (DiSC3(5) + PTZ, $p << 0.05$, ***), further confirming that the rapidly increasing FL signal corresponds to voltage changes in the brain associated with seizures.

The epilepsy group displayed a significant signal augmentation within 30 min following the seizure episode. The CR of FL ($\Delta F/F_0$) was calculated, revealing that the epilepsy group had a CR of over 9%, approximately four times higher than the other two groups (Figure 4e). Although the ratio is not as high as other fluorescent imaging rates,[33] it still provides sufficient sensitivity and contrast for voltage dynamics screening. Furthermore, if specific regions are targeted, FL should allow for the detection of CRs reaching a few tens of percent, rather than using the entire brain ROI. It should be noted that while small animal FL imaging technology offers a wide FOV, its application is limited by its relatively low resolution and lengthy acquisition time. Consequently, we were only able to evaluate the duration of epileptic convulsions on a minute scale and were unable to precisely pinpoint the specific brain regions where seizures occur. Therefore, there is a need for improved localization techniques with higher spatial and temporal precision to better detect neuronal electrical activities.

2.5. PA-VSD Visualizes Electric Neuroactivity In Vivo

PA imaging has proven to have great potential in achieving higher spatial and temporal resolutions for brain monitoring. We set up two groups for the PA experiments: a control group that received a saline injection, and an epilepsy group that received a PTZ injection. To allow sufficient time for DiSC3(5) to enter the brain through systemic circulation and achieve stabilized distribution, we initially observed the signals for two hours before inducing acute seizures in mice. The PA signal was low

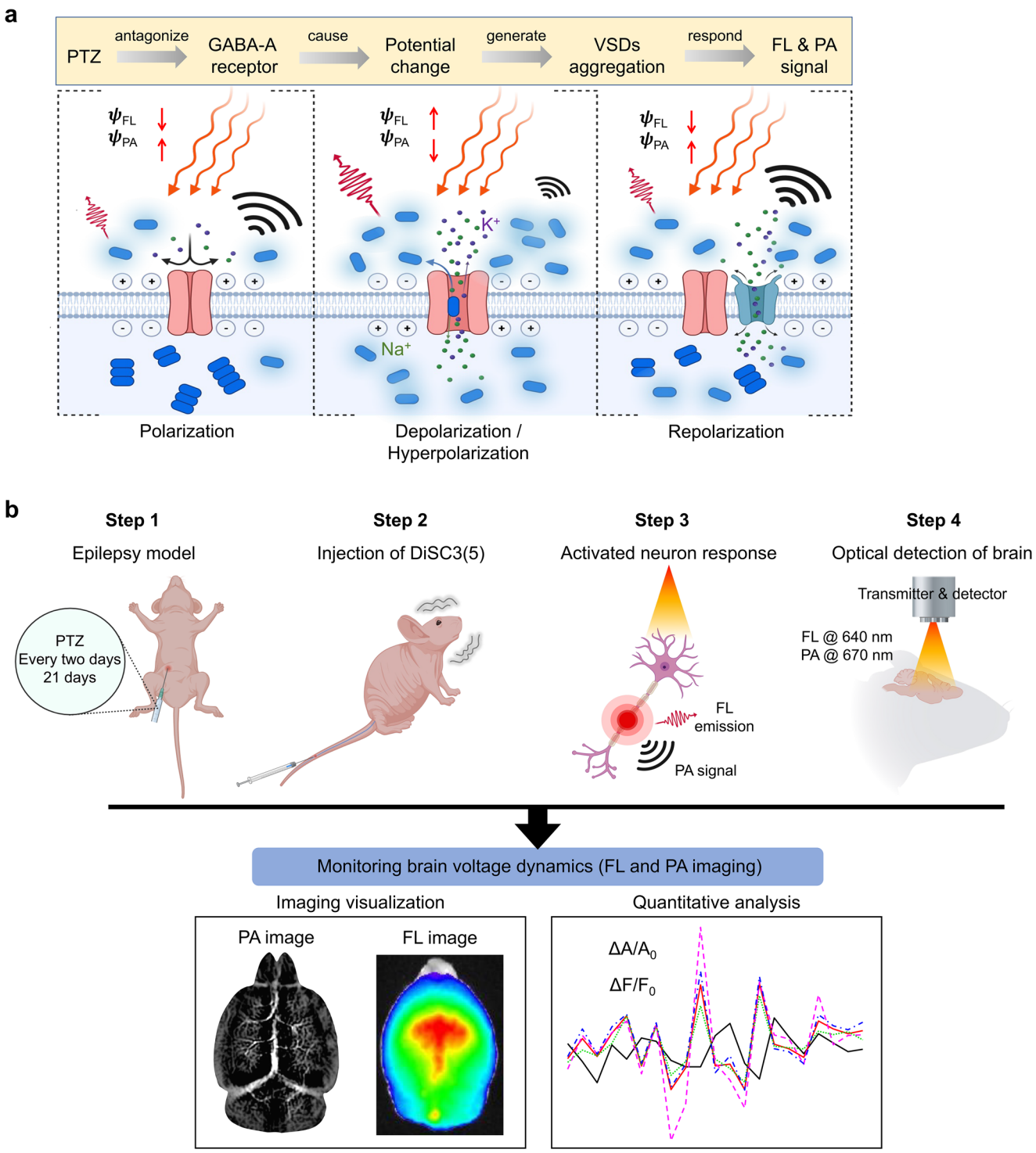

Figure 3. The mechanism of DiSC3(5) responding to voltage a) and the workflow of in vivo electrodynamics monitoring in an epilepsy mouse model b). DiSC3(5), a cationic VSD, penetrates the phospholipid bilayer of the neuronal cell membrane and polymerizes under negative potentials, which results in temporarily quenching the FL signal while enhancing the PA signal. When the discharge reaction triggers a de- or hyperpolarization state, which drives the dye to scatter as monomers, they regain the FL signal and decrease the PA signal until repolarization. PTZ is an epilepsy-inducing drug. ψ_{FL} and ψ_{PA} represent the intensity values of the FL and PA signals, $\Delta F/F_0$ and $\Delta A/A_0$ are the CR of ψ_{FL} and ψ_{PA}, respectively.

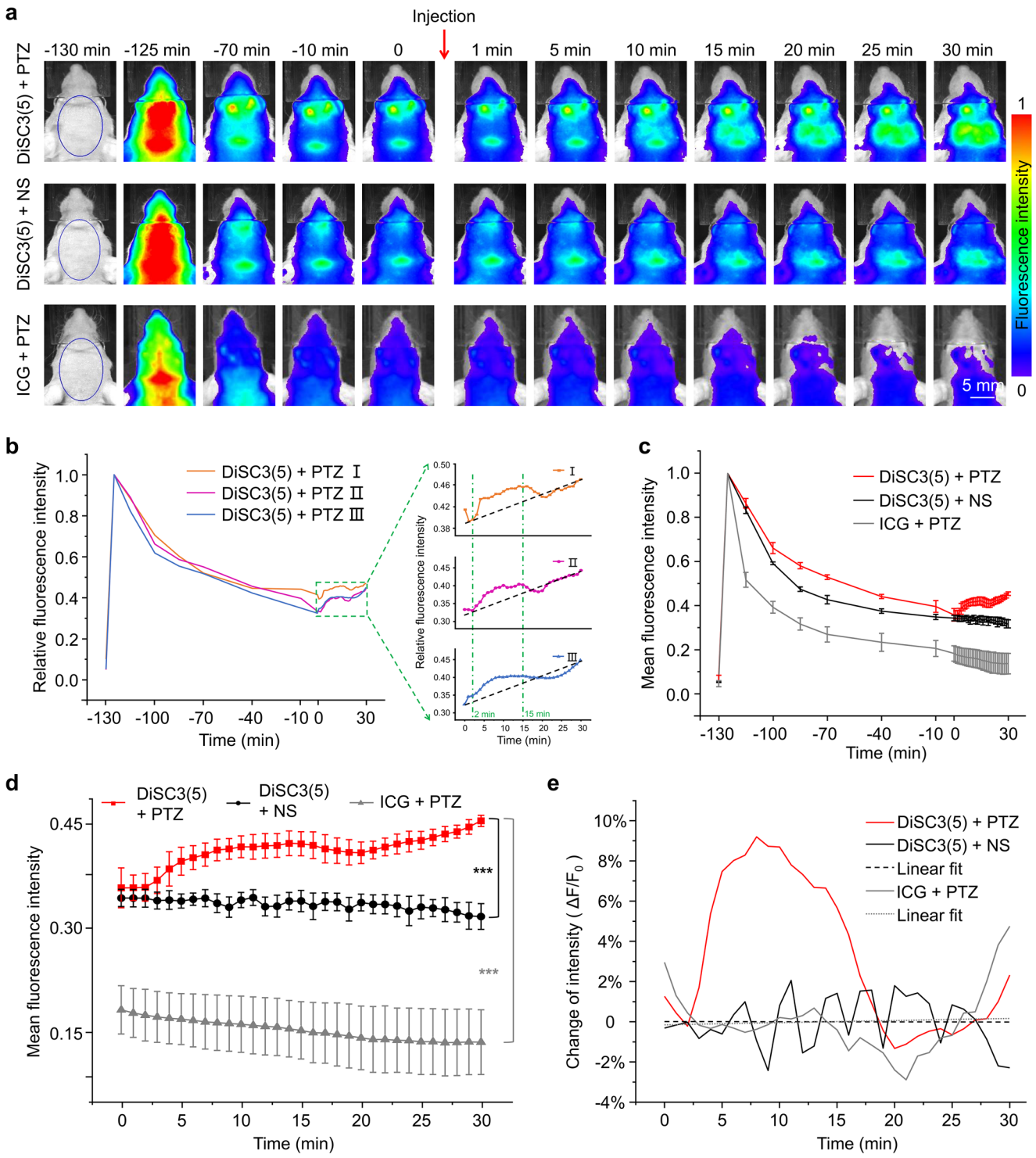

Figure 4. FL imaging of epileptic mouse brain based on DiSC3(5). All signals are normalized to a uniform level. a) FL Images of mouse brain voltage response. b) FL signal change curves of the experimental group (DiSC3(5) + PTZ). c) Quantitative statistical analysis of the ROIs shown in a. d) Quantitative statistical analysis of the mouse brain after injection. Experimental group has a significant difference from two control groups ($p << 0.05$: ***, detailed analysis data was shown in Table S1, Supporting Information). e) Temporal profiles of the proportionate increase in FL intensity in the mouse brain after injection. All the error bars are SEM.

at the beginning (i.e., −129th min in **Figure 5a**) due to the effect of discrete dyes and blood dilution. Thereafter, it gradually increased and reached a relatively steady state (−40–0 min, consistent with the FL results). Both FL and PA data indicate that VSDs require at least an hour and a half to establish a stable or resting condition, suggesting that they cannot be used to immediately detect voltage changes upon entering the organism. The slower rate of stabilization in the epileptic group compared to the control group is likely attributed to the pathological manifestations of the epilepsy model, which increase neuronal activity and hinder the dyes from reaching a steady state. The PTZ-induced seizures displayed more extreme signal changes than the control group, showing a somewhat significant difference ($0.001 < p = 0.0019 < 0.01$, **). However, the overall trend was also decreasing, which was consistent with the in-vitro test results (Figure 2j). These findings demonstrate that PA-VSD could detect seizures as early as 2 min in advance (Figure 5b, Zone 1), making it as sensitive as EEG monitoring (Figure S4a, Supporting Information). During the monitoring of epileptic activities, numerous large seizures occurred within a 30-minute period.

Since the brain voltage oscillations occur across multiple frequencies, the voltage flow associated with epilepsy consists of several waves with specific characteristics. Fourier transform is often performed to interpret the properties of obtained brain electric signals.[34,35] Analogously, the PA signal series were processed by Fourier transform to extract more correlations amongst these groups. As can be seen in Figure 5c, the epilepsy group had more high-frequency-amplitude components than the control group, similar to the high-frequency electrical signals observed in EEG monitoring during epileptic events. Regions d', e', and f', representing epileptic 1, epileptic 2, and normal status, were chosen for independent processing, and the results were shown in Figure 5d–f, respectively. Figure 5f does not display any discernible differences, indicating that the normal status does not exhibit the same high-frequency characteristics as the epileptic status. This provides further evidence that high frequency and high amplitude are distinctive features of epileptic signals. Therefore, by examining the frequency map of the PA signals, it is possible to spectrally separate the DiSC3(5)-induced voltage signal from the PA signals originating from normal tissues. This finding suggests the feasibility of detecting epilepsy and other electrical activities in the brain based on changes in the amplitude and spectrum of VSD-induced PA signals.

We calculated the CR ($\Delta A/A_0$) to validate epilepsy. In **Figure 6a**, we selected the time series in zone 2 (Figure 5b) as representative of epileptic activity (marked in red), zone 3 as the calm state (marked in blue), and corresponding regions in the control group (marked in black). We adopted the ±10% interval as the baseline range for defining epilepsy because the CR in control group was more consistent and most of the change was present in this interval. The presence of bottom peaks (< −10%) suggests the occurrence of seizures, as the electrical signal exhibits a photoacoustic weak signal characteristic. As observed, the epileptic group displays a significant difference compared to the control and calm groups. To further analyze the high-frequency components, the discrete Fourier transform was applied to extract the amplitude peaks, resulting in the production of the DHF matrix. Notably, the curves for $\Delta A/A_0$ and DHF exhibit similar trends, with a peak-to-peak overlap observed in the epilepsy group. Through our examination of their correlation (Figure 6b), we found a strong link between the CR and DHF factors. The asterisk peaks marked in red indicate more severe epileptic pulses. Consequently, a new methodology can be established by coupling the CRs and DHF of PA signals to screen epileptic sequences.

2.6. PA-VSD visualizes the Voltage Conduction Pathways with High Spatiotemporal Resolution

For further investigation, we chose Zone 2 with obvious seizures for functional connection analysis. We first displayed the PA images. The 'Gray' image is the original image reconstruction result ("0 s" in **Figure 7a**), and the 'Jet' is the pseudo color result for the deduction of the 0 s image matrix from that at the current time point. Given that we utilized the absolute value of the image matrix, a redder hue corresponds to a more negative value and a weaker signal. As seen, there was a noticeable increase in brain activity between the 5th and 13th seconds, with bright regions demonstrating the exact localization of the seizures. Starting from the 5th second, area 1 started to light up and rapidly transmitted to areas 2 as well as 3 at 7 s (Figure 7a). Then, the Allen Mouse Brain Atlas was used to identify 58 brain regions corresponding to PA brain images (Figure 7b) and make them separate ROIs.

210 frames of raw data were extracted, and the time series of the 58 ROIs were computed respectively. A two-by-two correlation analysis was carried out, shown in Figure 7c. Based on the association hotmap, the 58 brain regions could be divided into 7 categories. Sets 6 and 7 have relatively negative correlations since they are entirely composed of limbic brain regions or near the superior sagittal sinus (black dotted box in Figure 7c, e.g. 31, 44, 45, 29, 58 ROIs). The brain areas in sets 4 and 5 show modest correlations, suggesting that these are the much calmer regions in epilepsy and may not be involved in electrical signal transmission in this period. Electrical communication is more likely to occur in sets 1–3, which are the regions with substantial association. We were surprised to find that the active areas of the left hemisphere in Figure 7a coincide with the brain regions in Set 3. Those regions presented certain neighboring correlations and conductance. For instance, ROI 3-5-9-8-10-13-25 formed as an electrical signal transport channel. Combined with a high-temporal-resolution PA time profile, we can see the direction of transmission (red dotted arrow in Figure 7a,b). Next, we examined the temporal correlations of 13 brain regions in set 3 (Figure 7d). A great degree of coherence can be seen in all the periods, which may be attributed to coordinated and fast-transmitting electrical communication. Photoacoustic electroneuroimaging may identify not only the precise location of nerve impulses but also the pathway and orientation of signal conduction through high spatiotemporal visualization.

In specific locations, we calculated the CRs of three areas, respectively (from 5–13th seconds). The results showed that area 3 exhibited the strongest epilepsy compared to the others, which suggests the presence of the most severe epileptic foci, corresponding to ROI 24,25. Considering that surgical treatment has been effective for some epilepsy cases in the past years, this approach could potentially assist in guiding epilepsy surgery by providing a more precise localization of the active epileptic foci.

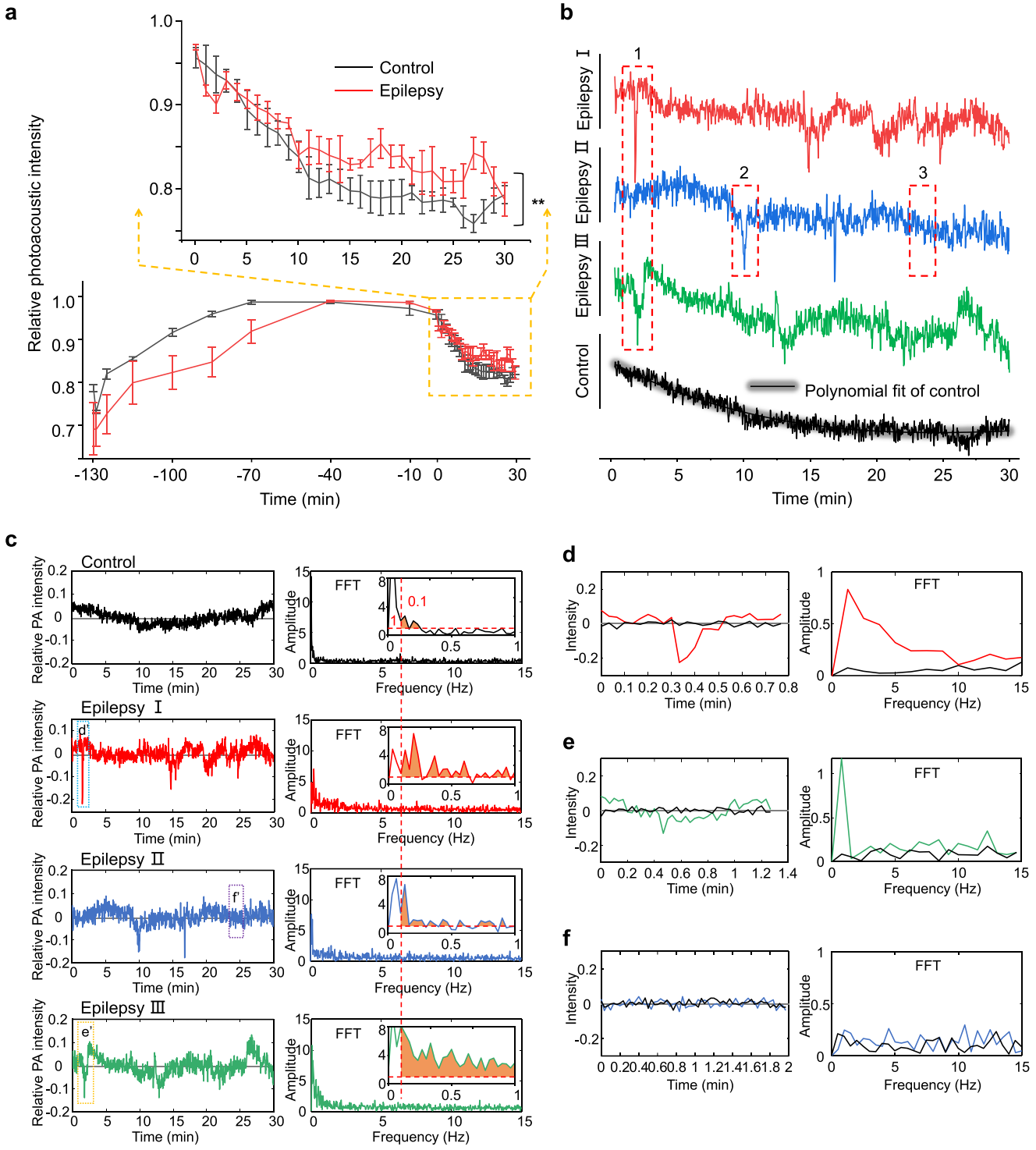

Figure 5. In-vivo PA-VSD monitoring of electrical activity in epileptic mouse brain. a) Comparison of whole brain PA signals in epilepsy and control groups. The yellow dashed box shows the signal changes after injection and the two groups have a significant difference ($0.001 < P = 0.0019 < 0.01$). The error bars are SEM. b) Temporal profiles of three epilepsy groups and the control group after injection. The control group is the mean data of three, and the black-shaded curve is its fitted curve. c-f) Fourier transform analysis of PA signals. c) is the time series representation of detrended PA signal and their corresponding frequency profiles for four groups (Frequency > 0.1 Hz and amplitude > 1). d-f) are the segmented PA signal selected in c and their frequency profiles.

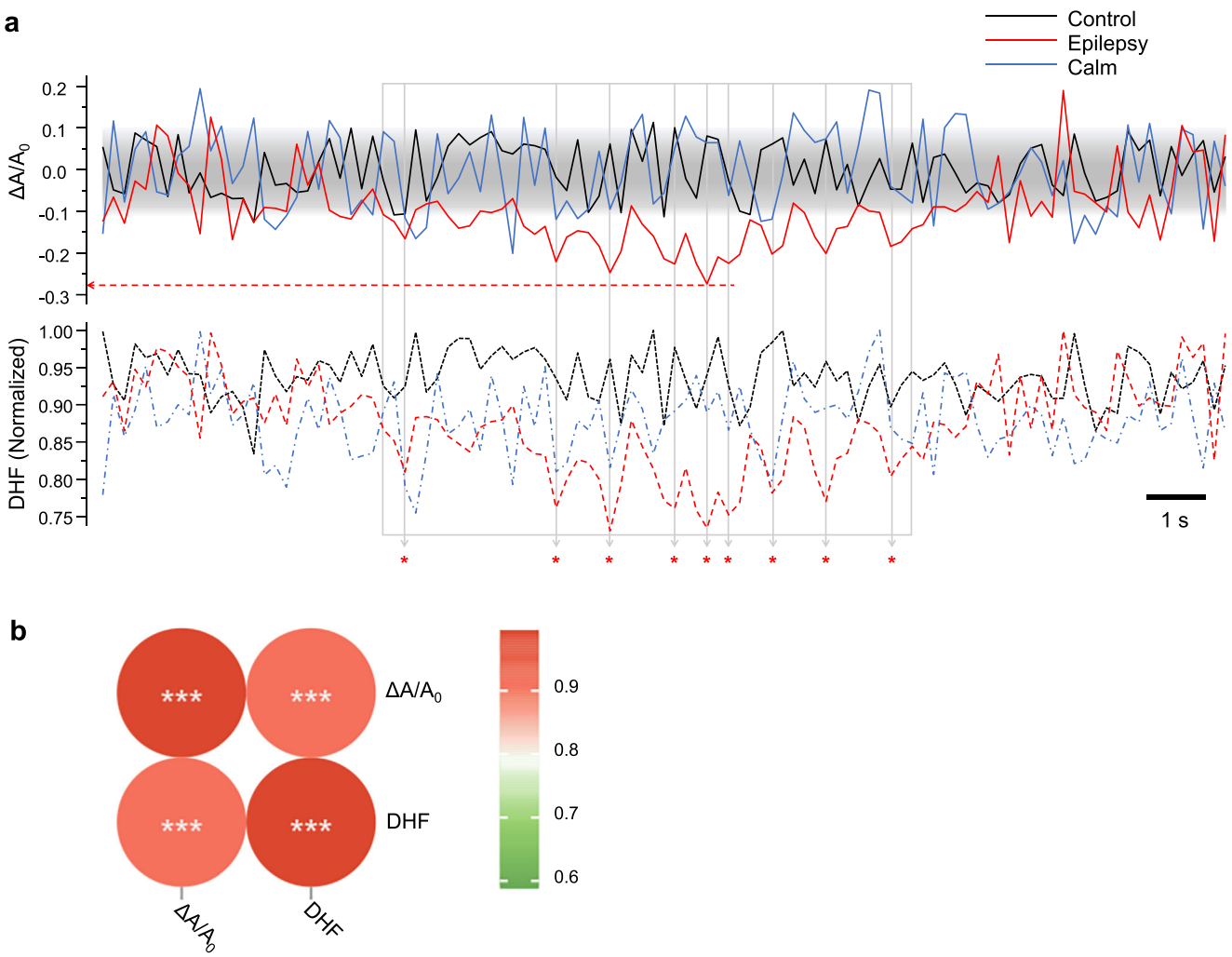

Figure 6. Quantitative analysis of PA signals, including the CRs and DHF factors. a) The $\Delta A/A_0$ and DHF curves. Two-peak overlapping spikes indicate more severe seizures, marked with a red '*'. b) Correlation hotmap of $\Delta A/A_0$ and DHF.

3. Conclusion

Optical imaging methods have gained significant popularity in neuroscience in recent years.[4,36,37] However, acquiring in vivo signals remains a critical challenge in optical brain imaging. Traditional methods for imaging mouse brains often involve invasive procedures such as skull thinning or craniotomies, which are not suitable for clinical applications.[38–41] Additionally, strong light scattering in brain tissue limits the generation of high-resolution images at deeper levels. Although shifting to longer excitation wavelengths, such as the Near-infrared II window, can increase penetration depth, specialized fluorophores only extend the depth limit to nearly one millimeter.[11] Therefore, there is still a need for the development of non-invasive, wide-field, deep-penetrating, high-resolution, high-speed, and in vivo brain imaging techniques.

In this work, VSD-type indicators are sought, whose optical properties are tailored to directly reflect electrical impulses or membrane potentials. These indicators have been widely used for assessing cell behavior, and their safety and photostability for biological use have been extensively investigated.[42–44] One example of VSD is DiSC3(5), which we experimentally confirmed to exhibit sensitive PA and FL responses, making it suitable for brain voltage detection. Unlike gene-encoded dyes, DiSC3(5) avoids ethical concerns in human trials and clinical validation. It directly responds to voltage changes by monitoring PA and FL signals, without relying on calcium ion concentration. Importantly, the ingestion of DiSC3(5) and exposure to light are harmless to living organisms. Furthermore, our FL and PA electrodynamic tests demonstrated that they exhibited sufficient photostability (>75%) for 30 min continuous monitoring. While full-field FL imaging offers excellent signal intensity sensitivity, its application for brain voltage monitoring is limited due to inadequate temporal and spatial resolution and the inability to provide depth information.

In contrast, PA imaging offers notable benefits and features to meet these criteria.[45–47] This work is the first trial to employ a high-spatiotemporal-resolution WF-PABD for prolonged monitoring and tracking of the VSD response to reflect brain activity in vivo. Specifically, a generalized VSD indicator DiSC3(5)

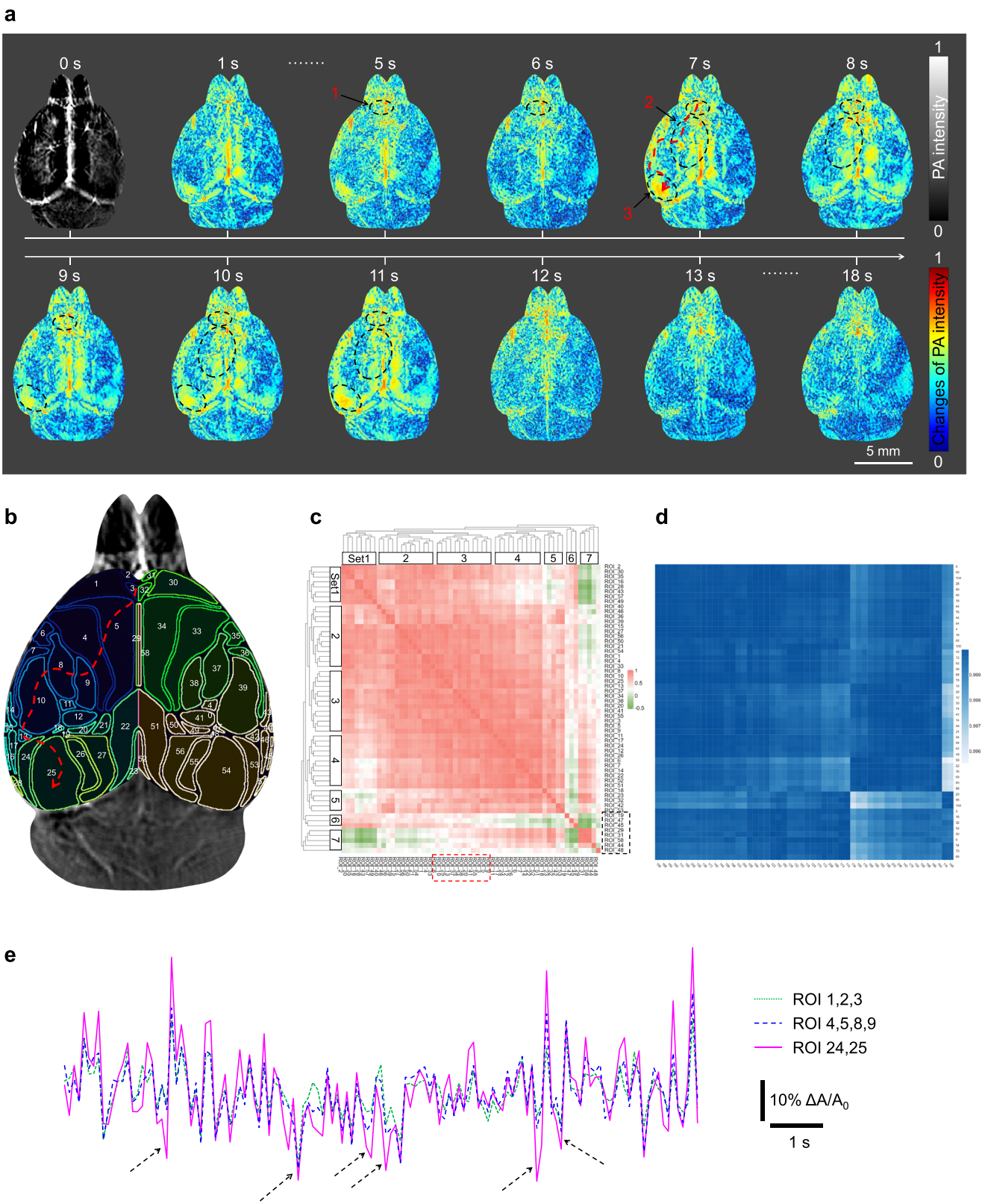

Figure 7. PA-VSD reveals the precise location of epilepsy dynamics, as well as the pathway and orientation of signal conduction. a) Photoacoustic reconstructed images exhibited in chronological order. The changes in PA intensity distribution indicate epileptic localization and the time series indicates the directionality of signal conduction. b) Photoacoustic image with brain regions, totaling 58 ROIs. c) Correlation analysis of two-by-two regions. d) 210-frame temporal correlation of 13 brain regions in set 3 (red dotted box in c). e) The time series of segmented 5–13th seconds, and their separated areas calculations. Area 1 correspond to ROI 1,2,3, area 2 correspond to ROI 4,5,8,9, and area 3 correspond to ROI 24,25.

was employed to conduct PA imaging under a single wavelength excitation of 670 nm, which is under a noticeably reduced blood absorption background and making the DiSC3(5) signal changes more representative of brain voltage variations. The designed platform can provide an effective FOV of ≈5 cm in diameter, which is adequate to image the entire mouse brain and potentially a portion of human brain.[48] Then this platform yields an ultrahigh acquisition speed of 10 µs per frame, which can overcome the motional artifacts and hence allows for monitoring under free motion status. Considering the time needed for data transmission and storage, 10 Hz imaging speed was obtained for rapid monitoring of dynamics. Collectively, in vitro cellular studies, fluorescent in vivo imaging, and EEG research were employed to support the analysis and forecast made by PA-VSD epilepsy monitoring system. In vitro experiments demonstrated the voltage response properties of DiSC3(5). The results show a clear increase in FL intensity and a decrease in PA intensity with growing level of depolarization. Similar signal enhancement was observed in fluorescence imaging of in vivo epileptic mice, significantly differing from the non-epilepsy and non-VSD groups, confirming that the signal changes during seizures were triggered by VSD. In addition, we used the classical PTZ induction method to construct a mouse epilepsy kindling model and performed EEG monitoring to assess the occurrence of epilepsy seizures. By employing PA-VSD, we can pinpoint the epileptic foci and determine regions with more active epilepsy activity, potentially providing guidance for surgical navigation and treatment. Interestingly, by combining high-temporal-resolution visualization and investigating brain region correlations, we obtained results on electrical conduction pathways and directions in certain regions, which can contribute to the study of nerve function and electrical conduction. Overall, we believe that the proposed PA-VSD framework can provide high-spatiotemporal-resolution visualization, accurate lesion localization, and valuable insights into brain function communication through whole-brain neuronal voltage activities, with far-reaching implications for in vivo neurophysiological investigations.

Nonetheless, there is still some space for improvement. For example, in the current configuration, the mouse's head is anesthetized and fixed in a precise position to maintain motionless in experiment, mainly due to the limitations of the structure and weight of the ring-piezoelectric-ultrasound transducer. The recent development of optical-fiber-based ultrasound sensors provides potential for future advancements toward in vivo monitoring of free-moving animals.[49,50] Moreover, the thick and opaque shells of large mammals and the human brain pose challenges for pulsed light penetration and the generation of PA signals with sufficient signal-to-noise ratio in situ. In this regard, switching to longer wavelengths (such as far infrared regimes) and combination with fast optical wavefront shaping solutions[51,52] will boost the penetration depth and show the potential for deep brain imaging. This work is an early endeavor to image and monitor the electrodynamics of brain disorders, such as epilepsy. With further engineering, the platform may pave the way for visualizing and investigating other voltage-related brain diseases, leading to impactful progress in fundamental and clinical neuroscience research.

4. Experimental Section

Voltage-Sensitive Dye Preparation: The molecular weight of DiSC3(5) is 546.53 and the powder was dissolved in DMSO at a concentration of 10 mM mother solution for use, then diluted with ultrapure water to a concentration of 100 µM for in-vivo animal brain experiments and diluted in cell medium at a concentration of 10 µM for in-vitro cell experiments for daily use only. To prevent bleaching of the dye, the dye preparation was carried out under low-light conditions and the solution container was covered with aluminum foil.

Animals and Ethical Statement: Male mice aged 9 to 12 weeks weighing 25 to 35 grams were used in the studies. The BALB/C- NUDE mice were purchased from Guangdong Medical Laboratory Animal Centre (China), and wild-type ICR mice were obtained from SPF (Beijing) Biotechnology Co., LTD. All mice were used to the typical laboratory conditions of humidity (55%), temperature (22.1 °C), 12-hour light/dark cycle, and full access to food and water. All animal experimental protocols were approved by the ethics committee of Guangdong Provincial People's Hospital (KY-N-2022-122).

Epileptic Mouse Model: Pentylenetetrazol (PTZ) is a GABA-A receptor antagonist. A single low-dose intraperitoneal injection of PTZ may elicit a mild seizure without convulsions, whereas a high dose in an animal may trigger a sudden, severe seizure and cause death. On the other hand, PTZ injections given repeatedly at low doses lower the threshold for convulsive seizures, so long-time low-dose PTZ therapy causes severe tonic-clonic epilepsy. Therefore, successive injections of a sub-convulsive dose have been used to develop a chemical kindling epilepsy mouse model.[53,54] PTZ-induced kindling in mice is an easy-to-use and well-accepted model for chronic epilepsy. Therefore, we selected this model for use in later studies, and the successful establishment of the model was also validated by in vivo EEG monitoring (Figure S4a, Supporting Information) and ex vivo tissue sections (Figure S5, Supporting Information).

The steps of the PTZ-induced epilepsy mouse model are as follows:

1) PTZ is dissolved in sterile 0.9 percent (w/v) NaCl at a concentration of 2.5 mg mL^{-1}. PTZ should be prepared on the day of usage.
2) Tag the mice and record their body weight for use.
3) Calculate the volume of PTZ solution for the injection based on the body weight of the mouse and the previously determined injection dose. The PTZ injection dosage is determined by the genotype and strain of the mouse. For the wild-type ICR mice, a PTZ injection dose of 35 mg kg^{-1} is used, while a more modest PTZ dose (1.8 mg kg^{-1}) is suggested for BALB/C-NUDE mice. So, when the ICR mouse weighs 30 g, 1.05 mg of PTZ is required, which means that 420 µL of a 2.5 mg mL^{-1} PTZ solution should be injected (35 mg kg^{-1} × 0.03 kg / 2.5 mg mL^{-1} = 0.42 mL), but a nude mouse of the same weight only needed to be injected with 216 µL (18 mg kg^{-1} × 0.03 kg / 2.5 mg mL^{-1} = 0.216 mL).
4) Use a 1-mL syringe and a 27-gauge needle to intraperitoneally inject PTZ into the animal's left or right abdominal region. Midline injections should be avoided. Avoid giving oneself the same shot many times.
5) After administering PTZ, place the animal in an observation chamber for habituation, and observe the behavior for 30 min. Then classify and score any anomalous behaviour, following the international certification of animal epilepsy grade criteria.
6) Inject PTZ every two days. 8–12 injections are usually enough, on average, to produce a successful model. Additionally, the injections can be discontinued early if the mice reach seizure level 5 or higher with three consecutive injections. This shows that the mice have been effectively modeled and are ready to be employed in the upcoming tests.
7) All injection procedures should be done between 14:00 and 18:00.

Characterization of DiSC3(5): Microplate readers (Spark, Tecan Austria GmbH, Austria) were used to measure the absorbance spectra. A standard curve was constructed with eight different concentrations of DiSC3(5) to assess the absorption curves spanning from 450 to 800 nm.

In Vitro Cell Experiments: In the cell experiments, HEK293T and Neuro-2a (N2a) cells were used. HEK293T were cultured in basic medium

(DMEM + 10% FBS + 1% P/S), and N2a were cultured in their special medium (MEM +10% FBS +1% P/S) at temperature of 37°C, humidity of 25–65 RH, and CO_2 content of 5%.

In CCK8 assays, each well in a 96-well plate was seeded with ≈2500 N2a cells respectively and 100 µL of the standard medium was added and then cultured for 4 h. The Control group did not add DiSC3(5), and the other 7 groups were added with 0.1, 0.5, 1, 1.5, 2, 3, and 5 µM DiSC3(5), respectively. The incubation was continued for 24 h, and the supernatant was removed, and then added 100 µL of 10% CCK8 reagent. Then continued incubation for 2 h. The absorption values were detected under the Microplate reader (excitation: 450 nm). There were 8 parallel samples in each group, two samples with large differences were removed, and the mean and SE of mean were calculated for 6 samples.

Six concentration gradients of K+ buffers were prepared, each representing a change in cell membrane potential of 0, 20, 40, 60, 80, and 100 mV calculated by the Nernst equation. This buffer was prepared by mixing 50 mM Hanks Balanced Salt Solution (137.93 mM NaCl, 5.33 mM KCl, 4.17 mM $NaHCO_3$, 0.441 mM KH_2PO_4, 0.338 mM Na_2HPO_4, 5.56 mM D-Glucose, pH of 7.1–7.5) and 20 mM Hepes solution at a ratio of 3:2, and then adding KCl crystal to achieve K+ concentration of 5.7, 32.9, 64, 98, 137, and 492 mM, respectively.

In the quantitative experiment of cell membrane potential, HEK293T cells were cultured in 18 Wells (three rows and six columns) in a 96-well plate. 6.7 µL 3 µM DiSC3(5) was added into each well (total volume was 200 µL) for 40 mins of co-incubation, then the cell culture medium was removed and 200 µL of extracellular medium with different K+ concentrations was added into each column. Then added nothing to the first line, 5 µL 10 µM Valinomycin (Val) to the second line, and 5 µL 1 mM Gramicidin (Gra) to the third line and put them into the Microplate readers to measure the UV absorption curve.

The same procedure was applied to the N2a FL experiment, but without Val and Gra, and eight parallel experimental groups were made. The 96-well plate was put into the IVIS Spectrum In vivo Imaging System (Perkin Elmer, USA) to measure the FL signal (excitation of 640nm, emission of 680nm). The IVIS Spectrum software was used to circle the ROI and calculate the trend of the FL signal with the change of the membrane potential.

Photoacoustic microscopy (PAM) (G2 OR-PAM, INNO LASER, China) was used to measure the PA signal changes of DiSC3(5) in neuron N2a. On the day before the experiment, 1 × 106 N2a cells were grown in glass pe-tri culture dishes (6 dishes) with a bottom diameter of 90 mm. On the same day, 70 µL 10 µM DiSC3(5) was added to the culture medium (total volume was 7 mL) and incubated for 40 mins. Then, extracellular buffers with different K+ concentrations were respectively added into 6 culture dishes after the supernatant was sucked out. In PAM imaging, cell signals were obtained using a green laser at a wavelength of 532 nm and an energy of 0.26 mW with a range of 200 mV signal channels. The images are 900 µm × 900 µm in size, with a pixel spacing of 3 µm. All the images were reconstructed in MATLAB with our self-developed imaging algorithm.

In Vivo Fluorescence and PA Imaging for Monitoring of DiSC3(5) Response in Epilepsy Mice: After an epileptic mouse was anesthetized in the chamber (isoflurane, 1% VOL, gas flow rate of 1 $cm^3\ s^{-1}$), the mouse was placed on a holding platform and its head was secured with ear rods, and then switched to a mask for prolonged respiratory anesthesia. An intravenous indwelling needle was inserted into the tail of the mouse in advance and then placed in the fluorescence apparatus (IVIS Spectrum In vivo Imaging System, Perkin Elmer, USA) to capture the head image "Before" (−130th min). Then, the mice were placed in the instrument after injecting 100 µL of a 100 µM DiSC3(5) solution through the tail vein at a rate of 20 µL min^{-1} using a microinjection pump. FL images continued to be acquired at the time points of 5 min (−125th min), 15 min (−115th min), 30 min (−100th min), 45 min (−85th min), 60 min (−70th min), 90 min (−40th min), and 120 min (−10th min) after the cycling of DiSC3(5). Then, a certain amount of 10 mg mL^{-1} of PTZ solution was injected intraperitoneally into the mice and continuous monitoring was performed every minute for 30 min. Finally, the head ROI information was extracted from the obtained time series images for quantitative analysis. The experimental procedure of PA-VSD was similar to FL imaging. In the in vivo experiments, we chose a PTZ injection volume that was 4 times higher than the modeling to induce seizures, since PTZ-induced epilepsy was suppressed by anesthesia, which was also validated by in vivo EEG (Figure S4b, Supporting Information).

Data Processing and Analysis: FL images and data were generated with IVIS software, and PA images were processed and analyzed using MATLAB 2021b. The data were presented as mean ± SEM (standard error of mean). In vivo results of FL and PA statistical analyses were performed with Mauchly's sphericity test, and the comparisons between distinct groups were done based on a two-way repeated measures analysis of variance (ANOVA) procedure in RStudio/2023.09.0+463. $\Delta A/A_0$ was calculated with the formula: $\Delta A/A_0 = (A_i\text{-}A_0)/A_0$, where A_i is the PA intensity at i_{th} time point, and A_0 is its corresponding linear fit value (same with the $\Delta F/F_0$). The correlation hotmap was generated with Pearson type by the OmicShare tools, a free online platform for data analysis (http://www.omicshare.com/tools). Some icons in the schematic were from BioRender. All curves were produced using Origin 2022.

Supporting Information

Supporting Information is available from the Wiley Online Library or from the author.

Acknowledgements

The authors acknowledge the support of the National Natural Science Foundation of China (NSFC) (81930048, 82372010), National Key R&D Program of China (2023YFF0715303), Guangdong Science and Technology Commission (2019BT02 × 105), Hong Kong Innovation and Technology Commission (GHP/043/19SZ, GHP/044/19GD), Hong Kong Research Grant Council (15217721, R5029-19, C7074-21GF), and Hong Kong Polytechnic University (P0038180, P0039517, P0043485, 1-CEB1). The authors also appreciate Dr. Tian Jin's assistance in identifying the brain regions in photoacoustic images.

Conflict of Interest

The authors declare no conflict of interest.

Author Contributions

W.P., L.N., and P.L. proposed the idea and designed the experiments. W.P. performed the experiments, collected raw data, analyzed the data, prepared the figures for the manuscript, and wrote the original manuscript. B.Z. and H.L. helped conduct part of the in vitro experiments. Y.Z., C.M.W., X.H., and T.Z. helped with the result discussion, text revision, and formatting. H.L. and L.W. supported with neurological advice. L.N. and P.L. funded and supervised the project. All authors contributed to the writing and proofreading of the manuscript. All authors have read and agreed to the published version of the manuscript.

Data Availability Statement

The data that support the findings of this study are available from the corresponding author upon reasonable request.

Keywords

high spatiotemporal resolution, intravital visualization, voltage-sensitive dye (VSD), whole-brain electrodynamics, whole-field photoacoustic brain detection (WF-PABD)

Received: February 1, 2024
Revised: May 13, 2024
Published online: May 23, 2024

[1] S. Liu, J. Parvizi, *Sci. Transl. Med.* **2019**, *11*, 7830.
[2] T. Bräuner, D. F. Hülser, R. J. Strasser, *Biochim. Biophys. Acta* **1984**, *771*, 208.
[3] H. M. Shapiro, *Methods Cell Biol* **1994**, *41*, 121.
[4] Q. Yu, X. Wang, L. Nie, *Chin. Chem. Lett.* **2021**, *32*, 1879.
[5] W. Fu, T. Sugai, H. Yoshimura, N. Onoda, *Neuroscience* **2004**, *126*, 1033.
[6] T. J. Sejnowski, A. Destexhe, *Brain Res.* **2000**, *886*, 208.
[7] W. Yang, R. Yuste, *Nat. Methods* **2017**, *14*, 349.
[8] C. Stosiek, O. Garaschuk, K. Holthoff, A. Konnerth, *Proc Natl Acad Sci* **2003**, *100*, 7319.
[9] M. T. Hasan, R. W. Friedrich, T. Euler, M. E. Larkum, G. Giese, M. Both, J. Duebel, J. Waters, H. Bujard, O. Griesbeck, *PLoS Biol.* **2004**, *2*, 163.
[10] T.-W. Chen, T. J. Wardill, Y. Sun, S. R. Pulver, S. L. Renninger, A. Baohan, E. R. Schreiter, R. A. Kerr, M. B. Orger, V. Jayaraman, *Nature* **2013**, *499*, 295.
[11] D. G. Ouzounov, T. Wang, M. Wang, D. D. Feng, N. G. Horton, J. C. Cruz-Hernández, Y.-T. Cheng, J. Reimer, A. S. Tolias, N. Nishimura, C. Xu, *Nat. Methods* **2017**, *14*, 388.
[12] K. D. Piatkevich, S. Bensussen, H.-A. Tseng, S. N. Shroff, V. G. Lopez-Huerta, D. Park, E. E. Jung, O. A. Shemesh, C. Straub, H. J. Gritton, M. F. Romano, E. Costa, B. L. Sabatini, Z. Fu, E. S. Boyden, X. Han, *Nature* **2019**, *574*, 413.
[13] L. V. Wang, S. Hu, *Science* **2012**, *335*, 1458.
[14] X. Wang, Y. Pang, G. Ku, X. Xie, G. Stoica, L. V. Wang, *Nat. Biotechnol.* **2003**, *21*, 803.
[15] W. Pang, Y. Wang, L. Guo, B. Wang, P. Lai, J. Xiao, *Front Bioeng Biotech* **2022**, *9*, 807633.
[16] Y. Zhou, X. Huang, J. Li, T. Zhu, W. Pang, L. Chow, L. Nie, L. Sun, P. Lai, *Pharmaceutics* **2022**, *14*, 2689.
[17] R. Chen, S. Huang, T. Lin, H. Ma, W. Shan, F. Duan, J. Lv, J. Zhang, L. Ren, L. Nie, *Nat. Nanotechnol.* **2021**, *16*, 455.
[18] X. Huang, W. Shang, H. Deng, Y. Zhou, F. Cao, C. Fang, P. Lai, J. Tian, *Appl. Mater. Today* **2020**, *18*, 100484.
[19] J. Lv, Y. Xu, L. Xu, L. Nie, *Radiology* **2021**, *300*, 89.
[20] S. R. Kothapalli, G. A. Sonn, J. W. Choe, A. Nikoozadeh, A. Bhuyan, K. K. Park, P. Cristman, R. Fan, A. Moini, B. C. Lee, J. Wu, T. E. Carver, D. Trivedi, L. Shiiba, I. Steinberg, D. M. Huland, M. F. Rasmussen, J. C. Liao, J. D. Brooks, P. T. Khuri-Yakub, S. S. Gambhir, *Sci. Transl. Med.* **2019**, *11*, 2169.
[21] A. A. Shemetov, M. V. Monakhov, Q. Zhang, J. E. Canton-Josh, M. Kumar, M. Chen, M. E. Matlashov, X. Li, W. Yang, L. Nie, D. M. Shcherbakova, Y. Kozorovitskiy, J. Yao, N. Ji, V. V. Verkhusha, *Nat. Biotechnol.* **2021**, *39*, 368.
[22] T. Jin, W. Qi, X. Liang, H. Guo, Q. Liu, L. Xi, *Laser Photonics Rev.* **2022**, *16*, 2100304.
[23] S. Gottschalk, O. Degtyaruk, B. Mc Larney, J. Rebling, M. A. Hutter, X. L. Deán-Ben, S. Shoham, D. Razansky, *Nat. Biomed. Eng.* **2019**, *3*, 392.
[24] Z. Liu, X. Lu, V. Villette, Y. Gou, K. L. Colbert, S. Lai, S. Guan, M. A. Land, J. Lee, T. Assefa, *Cell* **2022**, *185*, 3408.
[25] D. Huber, D. A. Gutnisky, S. Peron, D. H. O'connor, J. S. Wiegert, L. Tian, T. G. Oertner, L. L. Looger, K. Svoboda, *Nature* **2012**, *484*, 473.
[26] R. Matthes, M. Feychting, R. Croft, A. Green, K. Jokela, J. C. Lin, C. Marino, A. P. Peralta, R. Saunders, K. Schulmeister, *Health Phys.* **2013**, *105*, 271.
[27] V. P. Zharov, E. I. Galanzha, E. V. Shashkov, N. G. Khlebtsov, V. V. Tuchin, *Opt. Lett.* **2006**, *31*, 3623.
[28] A. P. Singh, P. Nicholls, *J. Biochem. Biophys. Methods* **1985**, *11*, 95.
[29] G. Boix-Lemonche, M. Lekka, B. Skerlavaj, *Antibiotics* **2020**, *9*, 92.
[30] P. J. Sims, A. S. Waggoner, C.-H. Wang, J. F. Hoffman, *Biochemistry* **1974**, *13*, 3315.
[31] H. K. Zhang, P. Yan, J. Kang, D. S. Abou, H. N. Le, A. K. Jha, D. L. Thorek, J. U. Kang, A. Rahmim, D. F. Wong, *J. Biomed. Opt.* **2017**, *22*, 045006.
[32] L. Xi, T. Jin, J. Zhou, P. Carney, H. Jiang, *Neuroimage* **2017**, *161*, 232.
[33] X. L. Deán-Ben, G. Sela, A. Lauri, M. Kneipp, V. Ntziachristos, G. G. Westmeyer, S. Shoham, D. Razansky, *Light: Sci. Appl.* **2016**, *5*, 16201.
[34] U. R. Acharya, S. Vinitha Sree, G. Swapna, R. J. Martis, J. S. Suri, *Knowl Based Syst* **2013**, *45*, 147.
[35] M. Murugappan, S. Murugappan, in *2013 IEEE 9th International Colloquium on Signal Processing and its Applications*, IEEE, Kuala Lumpur **2013**, 289.
[36] X. Zhu, Y. Xia, X. Wang, K. Si, W. Gong, *Neurosci Bull* **2017**, *33*, 95.
[37] P. Osten, T. W. Margrie, *Nat. Methods* **2013**, *10*, 515.
[38] J. T. Trachtenberg, B. E. Chen, G. W. Knott, G. Feng, J. R. Sanes, E. Welker, K. Svoboda, *Nature* **2002**, *420*, 788.
[39] A. Holtmaat, T. Bonhoeffer, D. K. Chow, J. Chuckowree, V. De Paola, S. B. Hofer, M. Hübener, T. Keck, G. Knott, W. C. Lee, R. Mostany, T. D. Mrsic-Flogel, E. Nedivi, C. Portera-Cailliau, K. Svoboda, J. T. Trachtenberg, L. Wilbrecht, *Nat. Protoc.* **2009**, *4*, 1128.
[40] H. T. Xu, F. Pan, G. Yang, W. B. Gan, *Nat. Neurosci.* **2007**, *10*, 549.
[41] J. Grutzendler, G. Yang, F. Pan, C. N. Parkhurst, W. B. Gan, *Cold Spring Harbor Protoc* **2011**, *2011*, 065474.
[42] L. Linares-Hernández, A. M. N. Guzmán-Grenfell, J. J. Hicks-Gomez, M. T. González-MartıŃez, *Biochim. Biophys. Acta, Biomembr.* **1998**, *1372*, 1.
[43] S. V. Hrynevich, T. G. Pekun, T. V. Waseem, S. V. Fedorovich, *Neurochem. Res.* **2015**, *40*, 1188.
[44] J. A. Alvarez-Bustamante, V. V. Lemeshko, *Eur. Biophys. J.* **2016**, *45*, 815.
[45] T. Sun, J. Lv, X. Zhao, W. Li, Z. Zhang, L. Nie, *Photoacoustics* **2023**, *34*, 100569.
[46] L. Li, L. Zhu, C. Ma, L. Lin, J. Yao, L. Wang, K. Maslov, R. Zhang, W. Chen, J. Shi, L. V. Wang, *Nat. Biomed. Eng.* **2017**, *1*, 0071.
[47] S. K. Kalva, X. L. Deán-Ben, M. Reiss, D. Razansky, *Nat. Protoc.* **2023**, *18*, 2124.
[48] S. Na, J. J. Russin, L. Lin, X. Yuan, P. Hu, K. B. Jann, L. Yan, K. Maslov, J. Shi, D. J. Wang, C. Y. Liu, L. V. Wang, *Nat. Biomed. Eng.* **2022**, *6*, 584.
[49] J. Zhou, J. V. Jokerst, *Photoacoustics* **2020**, *20*, 100211.
[50] X. Zhong, Y. Liang, X. Wang, H. Lan, X. Bai, L. Jin, B.-O. Guan, *Light: Sci. Appl.* **2024**, *13*, 5.
[51] P. Lai, L. Wang, J. W. Tay, L. V. Wang, *Nat. Photonics* **2015**, *9*, 126.
[52] Z. Yu, H. Li, T. Zhong, J. H. Park, S. Cheng, C. M. Woo, Q. Zhao, J. Yao, Y. Zhou, X. Huang, W. Pang, H. Yoon, Y. Shen, H. Liu, Y. Zheng, Y. Park, L. V. Wang, P. Lai, *Innovation* **2022**, *3*, 100292.
[53] A. Dhir, *Curr Protoc Neurosci* **2012**, *58*, 9.
[54] E. Samokhina, A. Samokhin, *Int J Neurosci* **2018**, *128*, 1086.